ISSN (Print) 1226-1750
ISSN (Online) 2233-6656
Journal of Magnetics 25(2), 121-125 (2020) https://doi.org/10.4283/JMAG.2020.25.2.121

Structure and Magnetic Properties of Multiferroic $DyMnO_3$ Epitaxial Thin Films Grown on Different Substrates

W. T. Wang*

Institute of Opto-Electronic Information Science and Technology, Yantai University, Yantai 264005, P.R. China

(Received 3 February 2020, Received in final form 8 May 2020, Accepted 12 May 2020)

Fabrication of thin films is crucial in the study of fundamental properties of matter and designs of devices. In this work, multiferroic dysprosium manganites $DyMnO_3$ thin films were grown epitaxially on $SrTiO_3$ (001) and yttrium stabilized zirconia (111) [YSZ (111)] substrates by pulsed laser deposition technique. The fabricated films showed perfectly orthorhombic crystallization on $SrTiO_3$ (001) and hexagonal crystallization on YSZ (111) substrates. At low temperatures, the magnetic measurements revealed three magnetic transitions at 10 K, 21 K and 43 K for orthorhombic $DyMnO_3$ film, 7 K, 38 K and 58 K for hexagonal $DyMnO_3$ film, respectively. The results are consistent with those observed in bulk materials, corresponding to magnetic ordering of the Dy^{3+} ion spins, antiferromagnetic transitions and spin reorientation respectively. This work provides a convenient method to manipulate the film structure by choosing suitable substrates, and it can be used in the study of magnetic properties of multiferroic manganites and related device fabrication.

Keywords : multiferroic, magnetic properties, $DyMnO_3$ thin films, epitaxial

1. Introduction

The crystal structure and magnetoelectric properties of multiferroic rare-earth manganites $RMnO_3$ (R = lanthanide) have been studied for over 50 years, and the effects of atomic substitution on phase structure, magnetic and dielectric properties have been reported [1]. Due to the coupling or connection of ferroic orders, the manganites $RMnO_3$ are promising materials for applications in advanced technology, like the application in non-volatile memory devices, ferroelectric gates and so on [2-4].

Conventionally, these materials crystallize in two types of structures: orthorhombic and hexagonal. The perovskite orthorhombic Pnma structure is based on a three dimensional network of corner shared MnO_6 octahedra [5], while the hexagonal manganites with a space group $P6_3cm$ consist of dense oxygen-ion packing with Mn^{3+} ions having five-fold trigonal bipyramidal coordination, and R^{3+} having seven-fold monocapped octahedral coordination [6]. The different crystalline structures are strongly dependent on the radius of the rare earth ions. For larger ionic size, $RMnO_3$ adopts an orthorhombic distorted perovskite structure, like $LaMnO_3$, $GbMnO_3$, $TbMnO_3$, while for smaller rare earth cation, $RMnO_3$ tends to take a hexagonal structure, like $HoMnO_3$, $LuMnO_3$, $YMnO_3$. Under normal conditions, $DyMnO_3$ (DMO) crystallizes in an orthorhombic structure, although a metastable hexagonal phase can also be prepared by means of special synthesis methods, such as by firing under ultra-high-purity argon [7].

In the process of film preparation, pulsed laser deposition (PLD), chemo-mechanical polish lithography [8, 9], and reverse growth method [10, 11] are crucial techniques in the studies of fundamental properties of matter such as superconductivity [12-15], and sensing and quantum control [16, 17]. In this paper, we investigated the characteristics of the DMO films grown on different substrates by using PLD technique. The films crystallized in either orthorhombic or hexagonal structures depending on the lattice matching relationship between the substrates and the films. The magnetic properties of DMO films with different structures were studied by a superconducting quantum interference device (SQUID) magnetometer.

2. Experiments

The DMO thin films were fabricated on $SrTiO_3$ (STO) and Y_2O_3:ZrO_2 (YSZ) substrates by PLD using a Lambda

*Corresponding author: Tel: +86-135-7351-2787
Fax: +86-535-6901947, e-mail: whetwang@163.com

Physic KrF excimer laser (248 nm). The ceramic DMO target was prepared through standard solid-state reaction process. The stoichiometric Dy_2O_3 and MnO_2 with an analytic reagent grade of purity were used as starting raw materials. After milling and calcining, the resulting compounds were characterized by powder x-ray diffraction (XRD) using a Rigaku diffractometer with Cu $K\alpha$ radiation at 1.54 Å. Compressed pellet used as a PLD target was sintered at 1400 °C for 12 hours.

In order to obtain DMO films with different structures, STO (001) and YSZ (111) single crystals (0.5 mm in thickness) were used as substrates which were held at 700 °C during the process of PLD. The temperature was measured from the front side of the substrate holder. The deposition was performed under an oxygen pressure of 30 Pa to reduce the possible oxygen defects in DMO films. After 30 min in situ annealing, the deposited thin films were cooled down to room temperature with a rate of –5 °C/minute. The thickness of the fabricated DMO thin films was determined to be about 150 nm by a surface profile measuring system. The structures of the deposited DMO films were studied by XRD. The azimuthal φ scans were recorded in order to assess the phase purity and the epitaxial relationship between the films and the substrates.

The magnetic properties of the fabricated DMO films with different structures were analyzed by a SQUID magnetometer. The temperature dependent magnetization data were collected in both zero field cooled (ZFC) and field cooled (FC) modes in a temperature range of 2-300 K under a 200 Oe applied magnetic field.

3. Results and Discussion

The XRD pattern of the synthesized DMO ceramics is shown in Fig. 1. The measurement was carried out on powdered sample in the angular range of $20° \le 2\theta \le 70°$. The bottom vertical lines indicate the allowed Bragg reflections. The location and intensity of all the reflection peaks could be indexed to an orthorhombic structure without any detectable impurity implying the single phase of the prepared sample within the detection limits of the diffractometer. The XRD data were analyzed using Rietveld refinement method, and the calculated lattice parameters of the orthorhombic DMO were obtained to be a = 0.581 nm, b = 0.527 nm and c = 0.739 nm. The lattice parameters are comparable to that of JCPDS card No. 25-0330.

Generally, the fabricated films have the same structure as that of the target using in PLD process. Although the DMO target is orthorhombic, due to the pinning effect of the substrates, orthorhombic or hexagonal DMO thin films can be prepared conveniently by choosing suitable substrates. Figure 2 shows the typical θ-2θ XRD result of the DMO film grown on STO (001) substrate. As can be seen, besides the sharp (00l) diffraction peaks from the DMO thin film, no diffraction from randomly oriented grains or impurity phases can be detected from the x-ray pattern, suggesting that the prepared DMO thin film is in orthorhombic structure (o-DMO) and has a clear c-orientation on STO (001) substrate. The full-width-half-maximum (FWHM) values of the (002) reflection is about 0.4° indicating good out-of-plane texture. To investigate the in-plane texture, the φ scan around the (112) DMO reflection is shown in the inset of Fig. 2. The fourfold symmetry peaks reveal that the film is in orthorhombic structure and well aligned with the substrate. As the STO single crystal substrate is in cubic structure with lattice parameters of 0.3905 nm, the epitaxial relationship between o-DMO and STO (001) substrate can be determined as

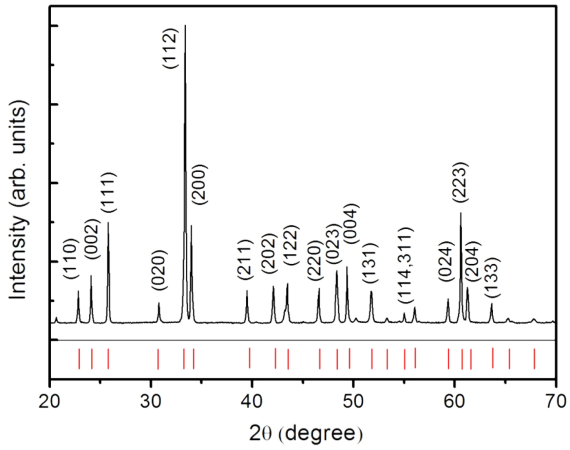

Fig. 1. (Color online) Typical θ-2θ XRD pattern with indices of lattice planes of DMO ceramics. Vertical lines at bottom indicate the allowed Bragg reflections.

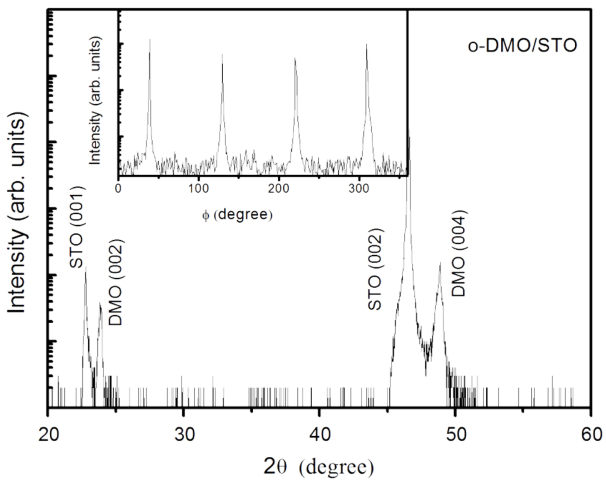

Fig. 2. XRD pattern of o-DMO film on STO (001) substrate. The inset shows the φ scan of the (112) peak of DMO film.

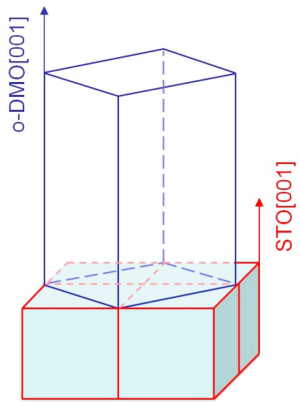

Fig. 3. (Color online) The schematic diagram of epitaxial relationship between the o-DMO film and STO (001) substrate.

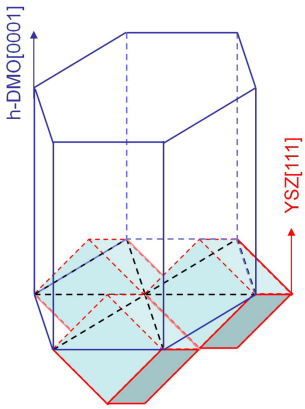

Fig. 5. (Color online) The schematic diagram of epitaxial relationship between the h-DMO film and YSZ (111) substrate.

[001] o-DMO // [001] STO and [010] o-DMO // [110] STO. The schematically epitaxial relationship is illustrated in Fig. 3. The lattice mismatches for the a- and b-parameters of o-DMO film with respect to the diagonal lines of the ab-plane of STO (001) substrate are expected to be –5.3 % along the [110] direction and 4.4 % along the [1$\underline{1}$0] direction of STO crystal. The calculation method of lattice mismatches was given in Ref. [18].

The XRD pattern of DMO film grown on YSZ (111) substrate by PLD using the same orthorhombic target is shown in Fig. 4. The film has a clear DMO (000*l*) orientation, which suggests the c axis is perpendicular to the surface of substrate. The φ scan of the (11$\underline{2}$2) peak is shown in the inset of Fig. 4. The XRD peaks and the sixfold symmetry reveal that the prepared DMO film is in hexagonal structure (h-DMO), and the in-plane epitaxial orientation of the film is derived as [11$\underline{2}$0] h-DMO // [110] YSZ. Fig. 5 shows the in-plane matching of the h-DMO film with the YSZ (111) substrate. As the lattice parameters of h-DMO are a = 0.618 nm and c = l.143 nm, and those of cubic YSZ are a = b = c = 0.514 nm, it is expected that the lattice mismatch for the in-plane lattice parameters between the h-DMO film and YSZ (111) substrate is approximately 1.8 %, leading to tensile strain in the film. The definition of lattice mismatch between the film and the substrate was reported previously [18].

Figures 6 and 7 display the magnetization (M) versus temperature (T) curves for o-DMO film and h-DMO film measured under ZFC and FC conditions, respectively. The applied magnetic field (200 Oe) is parallel to the films surface. Closed symbols are the data with the ZFC mode, while the open ones are for the FC mode. Above 100 K, the magnetization shows a slight change according to the Curie-Weiss law. At lower temperatures, M rapidly increases with decreasing temperature, indicating complicated temperature and magnetic field dependence of

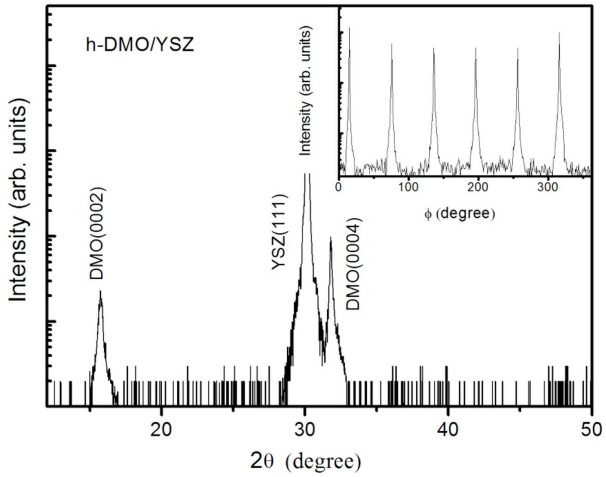

Fig. 4. XRD pattern of h-DMO film on YSZ (111) substrate. The inset shows the φ scan of the (11$\underline{2}$2) peak of h-DMO film.

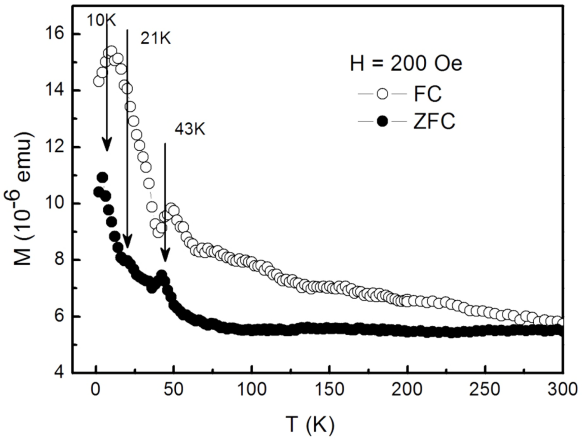

Fig. 6. Magnetization (M) vs temperature (T) plots of o-DMO film measured under ZFC and FC condition with an applied magnetic field of 200 Oe parallel to the film surface.

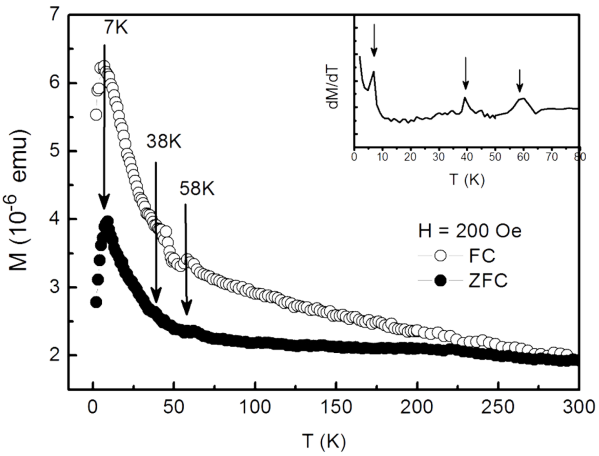

Fig. 7. Magnetization (M) vs temperature (T) plots of h-DMO film measured under ZFC and FC condition with an applied magnetic field of 200 Oe parallel to the film surface. A plot of the first order derivative of magnetization dM/dT with respect to temperature is displayed in the inset.

magnetization. In Fig. 6, both ZFC and FC curves of o-DMO film show anomalies close to 10 K, 21 K and 43 K at low temperatures. For bulk o-DMO materials, as is known, an antiferromagnetic transition of Mn^{3+} into the sinusoidalin commensurate phase at 40-45 K (denoted as T_N), an incommensurate-commensurate transition at 20-29 K (known as T_{lock}), and the magnetic ordering of the Dy^{3+} moments at below 10 K were reported previously [19, 20]. The three anomalies of the o-DMO film in Fig. 6 are almost consistent with those observed in bulk o-DMO materials and other orthorhombic rare-earth manganites [21, 22].

Temperature dependent of magnetization for h-DMO film is presented in Fig. 7. Three anomalies close to 7 K, 38 K and 58 K at low temperatures can be discerned, which represent the magnetic ordering of the Dy^{3+} moments, the incommensurate-commensurate transition and the sine-wave ordering of the Mn^{3+} moments, respectively. For clarity, the dM/dT curve in the temperature range of 2-80 K is shown in the inset of Fig. 7. The anomalies marked by arrows are at the same position with those in the main panel of Fig. 7. The results are comparable with the reported phase transition in bulk h-DMO crystals [23, 24]. Magnetic transitions of h-DMO film are different from those of o-DMO film. The different structures of orthorhombic and hexagonal DMO films are responsible for the observed different magnetic properties.

4. Summary

In conclusion, epitaxial o-DMO and h-DMO films were fabricated on STO (001) and YSZ (111) substrates, respectively, by PLD technique using an orthorhombic ceramic DMO target. The crystal structure and the epitaxial relationship between the films and the substrates were analyzed. At low temperatures, the films revealed three magnetic transitions, including magnetic ordering of the Dy^{3+} ion spins, the incommensurate-commensurate transition and the transition of antiferromagnetic phase into the sinusoidalin commensurate phase of the Mn^{3+} moments. The transition temperatures of o-DMO film are different from those of h-DMO film. The results suggest that the crystal structures have effects on the magnetic properties of rare-earth manganites. This work shows that epitaxial growth of thin films on suitable substrates can be used to obtain promising magnetic properties for multiferroic materials design.

References

[1] Q. Li, S. Bao, T. Hong, and J. Li, J. Magn. **23**, 5 (2018).
[2] N. Fujimura, T. Ishida, T. Yoshimura, and T. Ito, Appl. Phys. Lett. **69**, 1011 (1996).
[3] D. Ito, N. Fujimura, T. Yoshimura, and T. Ito, J. Appl. Phys. **93**, 5563 (2003).
[4] Umasankar Dash and Chang-Uk Jung, J. Magn. **23**, 345 (2018).
[5] J. B. Goodenough, Phys. Rev. **100**, 564 (1955).
[6] H. L. Yakel, W. C. Koehler, E. F. Bertaud, and E. F. Forrat, Acta. Cryst. **16**, 957 (1963).
[7] S. Remsen, B. Dabrowski, O. Chmaissem, J. Mais, and A. Szewczyk, J. Solid State Chem. **184**, 2306 (2011).
[8] M. Wang, R. Wu, J. Lin, J. Zhang, Z. Fang, Z. Chai, and Y. Cheng, Quantum Engineering **1**, e9 (2019).
[9] R. Osellame, Quantum Engineering **1**, e11 (2019).
[10] X. Sun, P. Wang, B. Sheng, T. Wang, Z. Chen, K. Gao, M. Li, J. Zhang, W. Ge, Y. Arakawa, B. Shen, M. Holmes, and X. Wang, Quantum Engineering **1**, e20 (2019).
[11] G. X. Miao, Quantum Engineering **1**, e21 (2019).
[12] P. Gao, W. T. Wang, W. Zhang, and Y. M. Sun, Sci. China Phys. Mech. **57**, 1875 (2014).
[13] W. Wang, Int. J. Mod. Phys. B **33**, 1950333 (2019).
[14] G. Zhou, Q. Zhang, F. Zheng, D. Zhang, C. Liu, X. Wang, C. Song, K. He, X. Ma, L. Gu, P. Zhang, L. Wang, and Q. Xue, Sci. Bull. **62**, 747 (2018).
[15] Z. Shao, Z. Zhang, H. Yuan, H. Sun, Y. Cao, X. Zhang, S. Li, H. Gedeon, T. Xiang, Q. Xue, and M. Pan, Sci. Bull. **63**, 1332 (2018).
[16] J. Zhang, X. Yu, G. Long, and Q. Xue, Sci. China Phys. Mech. **62**, 120362 (2019).
[17] D. E. Liu, Quantum Engineering **1**, e10 (2019).
[18] A. A. Bosak, C. Dubourdieu, J.-P. Senateur, O. Y. Gorbenko, and A. R. Kaul, Crystal Engineering **5**, 355 (2002).
[19] T. Kimura, G. Lawes, T. Goto, Y. Tokura, and A. P.

Ramirez, Phys. Rev. B **71**, 224425 (2005).
[20] N. Pavan Kumar and P. Venugopal Reddy, Mater. Lett. **122**, 292 (2014).
[21] M. Staruch, D. Violette, and M. Jain, Mater. Chem. Phys. **139**, 897 (2013).
[22] T. Arima, T. Goto, Y. Yamasaki, S. Miyasaka, K. Ishii, M. Tsubota, T. Inami, Y. Murakami, and Y. Tokura, Phys. Rev. B **72**, 100102(R) (2005).
[23] V. Yu. Ivanov, A. A. Mukhin, A. S. Prokhorov, A. M. Balbashov, and L. D. Iskhakova, Phys. Solid State **48**, 1726 (2006).
[24] S. Nandi, A. Kreyssig, J. Q. Yan, M. D. Vannette, J. C. Lang, L. Tan, J. W. Kim, R. Prozorov, T. A. Lograsso, R. J. McQueeney, and A. I. Goldman, Phys. Rev. B **78**, 075118 (2008).